A measurement of the energy and timing resolution of GlueX Forward Calorimeter using an electron beam

K. Moriya[a], J.P. Leckey[a], M.R. Shepherd[a], K. Bauer[a], D. Bennett[a], J. Frye[a], J. Gonzalez[b], S. J. Henderson[a], D. Lawrence[b], R. Mitchell[a], E. S. Smith[b], P. Smith[a], A. Somov[b], H. Egiyan[b]

[a]*Indiana University, Bloomington, IN 47405, USA*
[b]*Thomas Jefferson National Accelerator Facility, Newport News, VA 23606, USA*

arXiv:1304.4999v1 [physics.ins-det] 18 Apr 2013

Abstract

The performance of the GlueX Forward Calorimeter was studied using a small version of the detector and a variable energy electron beam derived from the Hall B tagger at Jefferson Lab. For electron energies from 110 MeV to 260 MeV, which are near the lower-limits of the design sensitivity, the fractional energy resolution was measured to range from 20% to 14%, which meets the design goals. The use of custom 250 MHz flash ADCs for readout allowed precise measurements of signal arrival times. The detector achieved timing resolutions of 0.38 ns for a single 100 mV pulse, which will allow timing discrimination of photon beam bunches and out-of-time background during the operation of the GlueX detector.

Keywords: GlueX, Jefferson Lab, calorimetry, lead glass, Flash ADC

1. Introduction

The upcoming GlueX Experiment [1] in Hall D at the Thomas Jefferson National Accelerator Facility (JLab) is an experiment that will primarily search for mesons with exotic quantum numbers. Meson states of interest will be produced using a photon beam incident on a proton target. It is crucial for the experiment to have a detector with good resolution and high acceptance for multi-particle events – studying the angular distributions of decay products is an essential tool in identifying underlying structure of the produced mesons. The Forward Calorimeter (FCAL) will be an essential detector for the experiment, providing energy measurements and timing information for photon showers in the forward region with polar angles $\theta < 12^\circ$ and energies between 100 MeV and 5 GeV.

In the fall of 2011, a 25-element miniature version of the FCAL was constructed for a beam test underneath the existing photon tagger of Hall B [2] at JLab. The main goals were to verify, as expected, that the hardware configuration of the FCAL modules would meet the desired energy and timing resolutions. While many studies with prototypes were performed during the design phase, this represented the first test of the production hardware and data acquisition system in a beam. Below we discuss the results of this beam test and compare them with previous measurements.

2. Setup of Experiment

2.1. FCAL components

The FCAL for the GlueX experiment consists of 2,800 lead glass modules, each coupled to its own type FEU 84-3 photomultiplier tube (PMT) and Cockcroft-Walton base (similar to that detailed in Ref. [3]). The lead glass blocks were equivalent to type F8 manufactured by the Lytkarino Optical Glass Factory [4], and each have transverse dimensions of 4×4 cm^2 and are 45 cm long. The Cherenkov light emitted by the electromagnetic showers produced within the lead glass blocks will be detected by the PMTs. The resulting PMT current pulses are digitized by 12-bit 250 MHz flash analog-to-digital converters (fADCs) designed by JLab [5]. Figure 1 shows an expanded view of one of the 2,800 FCAL modules.

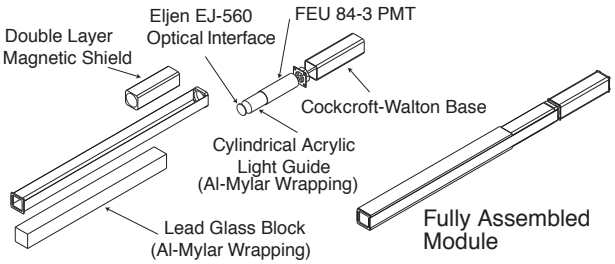


Figure 1: Expanded view of a single module of the GlueX FCAL.

The lead glass blocks and most of the PMTs are the same as those used in previous experiments, E852 at Brookhaven National Laboratory [6, 7] and the RadPhi Experiment at JLab [8, 9].

In the GlueX experiment, magnetic shielding of the PMTs is necessary due to the stray field of the solenoid magnet of up to 200 G. The PMTs are placed well within a double layer of soft iron and mu-metal shield. The light collection from the lead glass block to the PMT is facilitated using a cylindrical acrylic light guide glued to the PMT. An Eljen EJ-560 optical interface "cookie" is used to connect the guide to the lead glass block. The primary goal for this beam test is to verify that we

can achieve the design energy resolution at low energies, where statistical fluctuations in the number of Cherenkov photons detected dominate the resolution. This, in turn, would validate the design of the light collection system using optical photons with the characteristic Cherenkov angular distribution inside of the block, a task that had only been performed with ray-tracing simulation.

Besides measuring the energy of electromagnetic showers, the FCAL will measure the timing of the showers. During GlueX running, the JLab Continuous Electron Beam Accelerator Facility (CEBAF) beam will provide an electron beam bunch every 2 ns. Electrons in the bunch interact with a thin diamond crystal radiator to produce a linearly-polarized photon beam. During nominal running configuration the diamond is oriented so that the coherent bremsstrahlung process produces a peak in both linear polarization and photon flux at photon energies of about 9 GeV. The photon energy is measured by measuring the momentum of the recoil electron using the Hall D tagger. The photon rates are expected to be up to 10^8 s^{-1} in the coherent peak between 8.4 and 9.0 GeV, leading to a high rate of signal photons as well as electromagnetic background. The timing measurements of the FCAL will allow identification of the respective beam bunch that created the photon of interest and also help in reducing accidental backgrounds.

2.2. *Setup of Detector*

A 5 × 5 array of FCAL modules was constructed at Indiana University. The modules were encased in a light-tight aluminum body, with a gear drive that allowed the modules to be tilted at an angle so that the front face of the modules were perpendicular to the incoming electron trajectories. Figure 2 shows a drawing of the detector.

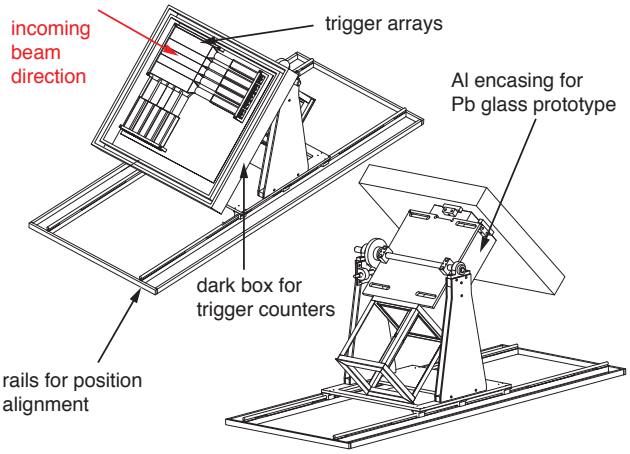


Figure 2: Drawing of the array from the front and back with the trigger box attached. For illustration purposes, the lid of the trigger box is shown open.

For triggering purposes, two arrays of five Eljen EJ-200 plastic scintillator paddles were placed at the front of the detector. The three inside paddles had widths of 4 cm, while the two outside paddles were 6 cm wide and used as veto signals to the trigger. The two arrays were oriented perpendicularly to each other, with the centers of each paddle centered on the border of two modules, as shown in Fig. 3. The scintillators spanned the length of the perpendicular array of modules. When looking into the detector from the upstream end (the "beam's eye view"), the horizontal paddles were labeled h1–h5 from the top, and the vertical paddles were labeled v1–v5 from the left. Each of the trigger paddles were optically connected to the same type FEU 84-3 PMTs used for reading out the detector modules. The signals from the PMTs were converted into NIM signals by a discriminator, and the digital output of the discriminators were recorded into the data stream using the same fADCs that were used for recording the pulse height of the lead glass modules. The trigger arrays were placed in a dark box that was attached to the front of the main detector. The dark box was made of 1.27 cm-thick plywood and painted black, with a thin (1.27 mm) aluminum plate underneath the trigger setup to hold the trigger paddles in place.

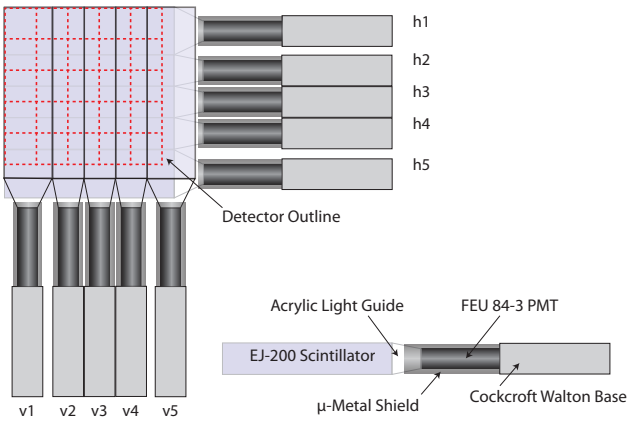


Figure 3: The placement of the trigger scintillator paddles on top of the modules. The position of the front face of the 5 × 5 array of detector modules is shown as the dashed lines.

In addition to the main trigger counters, there was a thin remote paddle located several meters upstream of the detector, along the nominal trajectory of electrons hitting the detector (shown in Fig. 5). The remote paddle was made of a 0.125 cm-thick plastic scintillator, wrapped in aluminized mylar, and connected to a Photonis XP2020 PMT. The signal was also converted into a NIM pulse signal using a discriminator and read out with a fADC channel. The purpose of this remote paddle was to identify electrons following the nominal electron trajectory during off-line analysis.

Figure 4 shows a diagram of our trigger logic, which was handled by standard NIM modules. The PMT pulses from each of the 25 modules within the detector array were digitized using a fADC. To trigger the readout of an event event to disk, we required a hit within at least one of the inside paddles from each array. The outside paddles were used as vetoes, and the veto signal was also individually recorded.

2.3. *Test Setup in Hall B*

The beam test was conducted within Hall B at JLab, which housed the CLAS detector and its photon tagger setup. Dur-

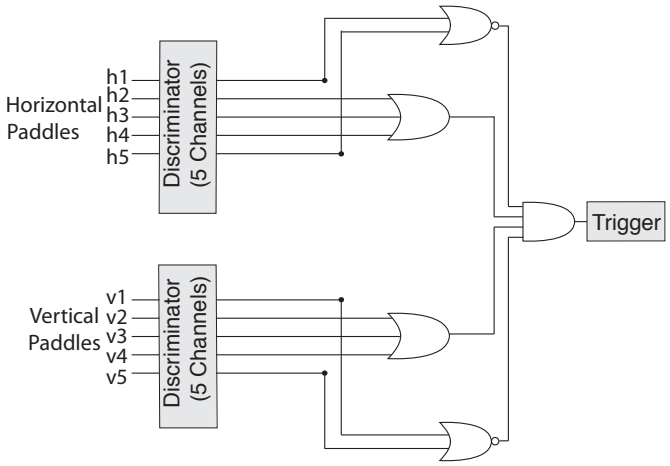


Figure 4: Electronics diagram for the trigger.

ing our beam test, the CLAS Collaboration was running the HD-ICE experiment with a real photon beam produced by bremsstrahlung, allowing us to use the electrons that had radiated photons. Our beam test was conducted parasitically to this run, and therefore we had no control over the beam energy or intensity. Figure 5 shows a schematic of Hall B and the tagger setup. The electron beam from the accelerator comes in from the left and is incident on a very thin radiator foil. Immediately following the radiator is the CLAS tagger magnet, which is a uniform-field dipole magnet. The electron trajectories are determined by the energy of the electron, and the position and angle at the exit of the magnet can be calculated. Details of the CLAS tagger setup can be found in Ref. [10].

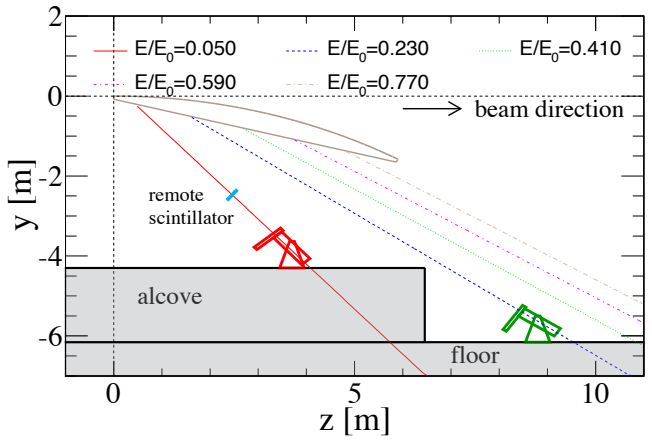


Figure 5: Schematic of the Hall B and the CLAS tagger system. The electron beam radiates a photon at coordinates $(0, 0)$. The trajectories of degraded electrons with varying energies are given by the lines originating from the vacuum exit window. Depictions of our detector are shown in the alcove area and floor.

The electrons exit the vacuum of the tagger magnet through a very thin exit window [11] and pass through the CLAS tagger detectors called the E-counters and T-counters. The E-counters are a plane of 384, 4 mm-thick plastic scintillators that detect the position of each electron for energy identification. The T-counters form a second plane of 2 cm-thick plastic scintillators that are used for timing identification of the electrons. The two detector planes are separated by 20 cm, and each counter within each plane is rotated so that it is facing normal to the incoming trajectory of electrons.

In our beam test, the detector was placed mainly in the area seen in the left side of Fig. 5 that we call the alcove. The detector was placed at the calculated location that intercepted electrons with 5% of the accelerator beam energy and was angled to face the incoming electrons. We also placed the detector in the floor area (right side of Fig. 5), where data were collected at a higher electron energy fraction. Due to mechanical interference and running constraints, we could not properly align the detector in the floor area, and hence did not use those runs for our energy resolution measurements (Sec. 3). However, since the timing resolution studies (Sec. 4) are not very sensitive to the detector alignment, we utilized these runs for this purpose, as they had the largest range of signal sizes.

3. Energy Resolution Study

3.1. Data Structure

For the energy resolution studies, our detector position was fixed and data were taken at three separate accelerator energies, allowing us to measure the energy resolution for these energies. The three runs that were used for our results had accelerator energies of 2.537, 4.446, and 5.542 GeV. Each run had approximately 2×10^5 events.

Each channel of the fADCs samples the PMT output voltage every 4 ns, and 50 samples were stored for each event. Figure 6 shows the read out samples from a single channel in one event. However, zero-suppression was implemented by setting a pre-programmed threshold and only channels that had at least one signal sample larger than this threshold were written to the output stream. The threshold applied to each channel was based on the pedestal, or baseline, which was measured without any input signals. The threshold was set to 10 ADC counts above the pedestal. Off-line studies showed that the resolution worsens with larger thresholds. After data taking, it was discovered that the thresholds for modules in the top two rows were inadvertently set much higher, leading to a significantly worse energy resolution. Therefore, the sub-sample of events with showers centered on these modules were not used in the determination of the energy resolution (see Sec. 3.4).

The module response to energy deposited in the lead glass is obtained by summing the pedestal-subtracted samples over a range of time. This range was optimized and was 20 samples (or 80 ns) starting at sample 9. The sum was performed off-line for the beam test, although for the GlueX experiment the determination of the signal size and time will be computed in Field-Programmable Gate Arrays (FPGAs) to manage the size of the output data stream.

The first step in our analysis was to ensure that we had a sample of events that had one and only one electron signal with the

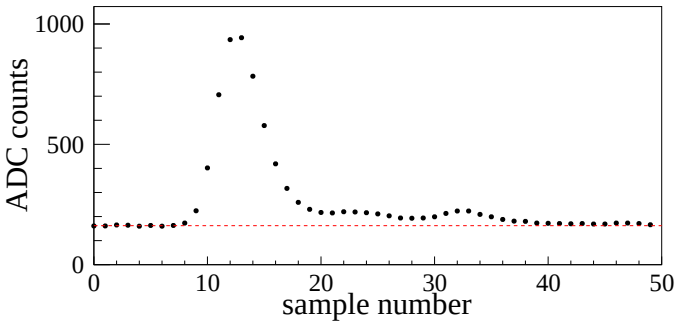


Figure 6: ADC values read out for one channel in one event. The pedestal which is given by the average of the first eight values is shown as the dashed red line. A clear signal is seen for this event.

correct timing. Therefore, a preliminary skim was applied to the data to extract such events. For each inside trigger scintillator, we determined the pedestal by taking the average of the first eight samples recorded. To exclude events that had an unstable pedestal, we removed events that had channels with a pedestal RMS greater than 2. This eliminated events that were on the tail of a previous event and also noise fluctuations at the beginning of the event.

Next, to ensure that the timing of the event was correct, the recorded NIM signals were examined and a coincidence in the leading edges was required. Also, events with a prolonged or second signal were removed. Finally, we required that only one horizontal and vertical trigger combination satisfied all of our trigger conditions to ensure that there were not two separate incoming electrons.

Similar requirements on the pedestal RMS and timing of the signal were made on the remote paddle based on the distribution of the data. We verified no signal was present on the veto just before or after the triggered events. For all detector modules, if any sample indicated an underflow or overflow in the ADC counts, that event was removed. The requirements on the trigger counters removed 10–20% of the data, while the requirements on the remote paddle removed 70–80% of our initial data sample indicating that our detector was frequently triggered by electrons that didn't pass through narrow angular range that was spanned by the remote paddle at the exit of the tagger window.

3.2. Gain Balancing Procedure

The total signal size for the event is given by summing the signals from all modules. For each run, the distribution of the total signal is fit with a Gaussian function and linear background. The width (σ) of this distribution divided by the centroid is then the measured resolution. Below we outline the procedure that was used to optimize the resolution consistently over all runs.

Prior to the beam test, the gain characteristics for the PMTs for each module were measured, and the high voltage (HV) settings were adjusted to equalize the gains. With these initial settings, data were taken to measure the initial energy resolution. A software gain balancing technique was then applied to minimize the event-to-event variance of the sum over all modules by scaling the signal size from each module by a constant module-dependent gain factor. This minimization can be formulated in terms of a Lagrangian multiplier method, which is described in detail in Ref. [8]. In Ref. [8] the mass squared of the π^0 and η mesons were used as constraints and measured differences from the meson masses squared were minimized. We fixed the average total signal size (in arbitrary units), and the standard deviation from this average was minimized. Such a problem is linear with respect to the gain factors and can be solved exactly, so that no iteration of the minimization is necessary. Next, using the computed gain factors, we adjusted the HV values based on knowledge of the gain characteristics of each PMT to better equalize the gains of the PMTs. Finally, we repeated the gain factor determination, and utilized these gain factors in our analysis.

We explored the stability of our software gain-balancing procedure by selecting events whose sum were within $\pm 3\sigma$ or $\pm 5\sigma$ of the mean and determined gain constants for both sets. This selection reduces the influence of non-Gaussian tails on the computation of the variance and the gain constants. Our results are therefore given as the average resolution from these selections, with an error given by half the difference, which is negligible on the scale of other systematic uncertainties in the determination of the energy resolution.

Figure 7 demonstrates the method of determining the resolution and shows the distribution of the total signal from all modules for two given runs at the same incoming electron energy. Figure 7(a) shows a run in which we used our initial HV settings without the PMT HV adjustments, and Fig. 7(b) is for a run when it was applied. For each case, the black hollow histogram is the distribution before the software gain balancing procedure is applied, and the gray (red online) hatched histogram is after. We see that software gain balancing is essential to obtaining optimal resolution, and the resolution is best when software corrections are applied to approximately equal-gain modules to start, *i.e.*, the precision that is lost when a low gain module is digitized by the fADC cannot be recovered by a simple multiplicative constant. In principle, one can continue to iterate hardware HV adjustments based on software gain constants; however, we performed only one such HV adjustment and utilized the software gain balancing procedure for all subsequently analyzed data.

3.3. GEANT Simulations

Corrections for energy loss and scattering in the material before the electrons entered the detector were determined using a GEANT4-based [12] simulation program. For each simulated data set, nominal energies for the electrons were chosen to correspond to actual electron energies used in the data collection. The fractional spread of the actual CEBAF electron beam is of order 0.01% and is negligible. Electrons were produced with energies centered around this value and with a range of ±10% to cover the range of rays that would scatter into our acceptance. For each event, the incident angle and position with which the electron exited the vacuum window were calculated based on

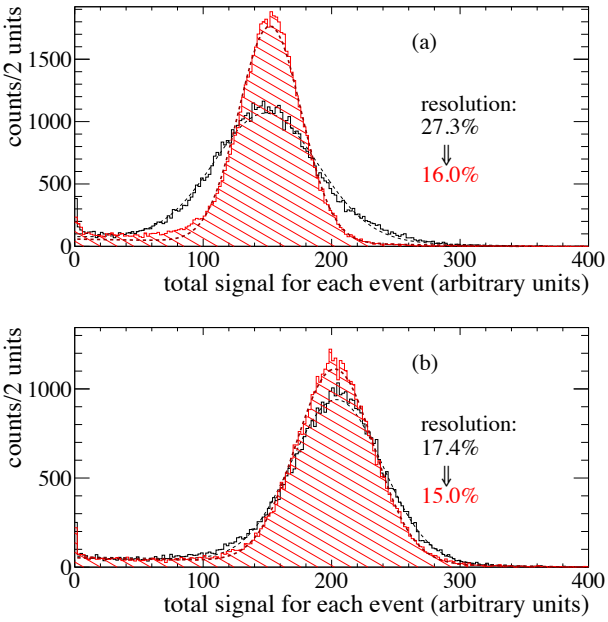


Figure 7: The distribution of the total signal of all modules before (hollow/black online) and after (hatched/red online) software gain balancing. Fits with a Gaussian function and linear background are shown by dashed lines. The two plots are from runs with the same electron energy; the top (bottom) plot is before (after) PMT HV adjustments. For the bottom plot, in addition to balancing gains, the overall average HV settings for the PMTs were raised, which increased the average total signal.

the CLAS tagger geometry. The electron energy distribution was modeled on a realistic bremsstrahlung distribution.

Using the simulation, we recorded the distribution of total incoming energy into our detector. The same trigger conditions as used in the analysis of the data were imposed on the simulated events. We fit the incoming energy distribution for our final selection of events with a Gaussian function to determine the mean and width. We concluded that the mean incoming energy into our detector was 12–14 MeV lower than the nominal energy with a spread of 4–6 MeV. Table 1 summarizes the results of our simulation for all energies. With the assumption that the intrinsic detector resolutions and the spread of energies add in quadrature, we can subtract this contribution to obtain the intrinsic detector resolution.

Table 1: Predicted energy and spread of electrons incident on the detector during three run periods. E_0 is the nominal incoming energy, while E and $\sigma_{\rm loss}$ are the center and width of the distribution obtained from the simulation, respectively.

E_0 (MeV)	E (MeV)	$\sigma_{\rm loss}$ (MeV)	$\sigma_{\rm loss}/E$ (%)
126.85	114.19 ± 0.03	4.54 ± 0.02	3.98
222.30	209.29 ± 0.05	5.15 ± 0.03	2.46
277.10	263.70 ± 0.04	5.70 ± 0.03	2.16

We incorporate these simulation results into our analysis in the following way. The spread in measured energies, $\sigma_{\rm meas}$, is the quadratic sum of the intrinsic detector resolution, $\sigma_{\rm det}$, and the spread due to different incoming energies, which we approximate with our simulation results, $\sigma_{\rm loss}/E$. With the assumption that the intrinsic detector resolution and the spread of energies adds in quadrature, we can remove the spread of energies to obtain the intrinsic detector resolution.

3.4. Energy Resolution

Figure 8 shows the energy resolution for five different trigger combinations. For all runs, the statistical uncertainties from the fits to determine $\sigma_{\rm meas}$ were negligibly small compared to the systematic variations observed by changing the analysis method. The dominant source of systematic uncertainty is variation in the performance of the individual modules. The nine different trigger possibilities, 3 horizontal × 3 vertical, could be analyzed independently and each trigger combination populates the individual modules differently. Therefore, the energy resolution varies with the location of the incident electron. Three trigger combinations were excluded due to the incorrect hardware threshold settings and a fourth combination was also excluded because it consistently gave poor resolution, although a clear reason was not identified. Each marker represents a different trigger combination, and have been shifted horizontally slightly for visual clarity. The measured energy resolution for the three electron energies of 114.2±4.5 MeV, 209.3±5.2 MeV, and 263.7 ± 5.7 MeV, as given by the average and standard deviation of the five trigger combinations, are 19.8 ± 0.5%, 14.3 ± 0.4%, and 14.1 ± 0.5%, respectively.

We expect that the dominant contribution to the resolution in this energy regime is statistical fluctuations in the number of photoelectrons produced in each PMT for each electron shower. Based on simulations of the light collection optics that were carried out in the design phase, the expected resolution of the GlueX FCAL can be parametrized as

$$\frac{\sigma}{E}(\%) = \frac{5.6}{\sqrt{E(\mathrm{GeV})}} + 3.5. \qquad (1)$$

This is shown as the solid blue curve in Fig. 8. Our energy resolution results are consistent with the design goal in this energy regime.

4. Timing Resolution Study

The second important performance metric of the calorimeter is the resolution of the absolute arrival time of the PMT pulse that is digitized by the fADCs. The fADCs for the FCAL sample the PMT pulses only every 4 ns; however, it is possible to utilize several samples and knowledge about the pulse shape to determine a pulse time with resolution much better than 4 ns. In a previous article [13], the timing resolution of the fADCs was tested using a pulsed LED source, and a timing resolution of less than 1 ns was determined for pulse heights of 100 mV and higher. In the following, we apply the same methods as in Ref. [13] for the purpose of confirming that we can obtain adequate timing resolution using actual electromagnetic showers. For this analysis, we utilize a single run with 507,828 events

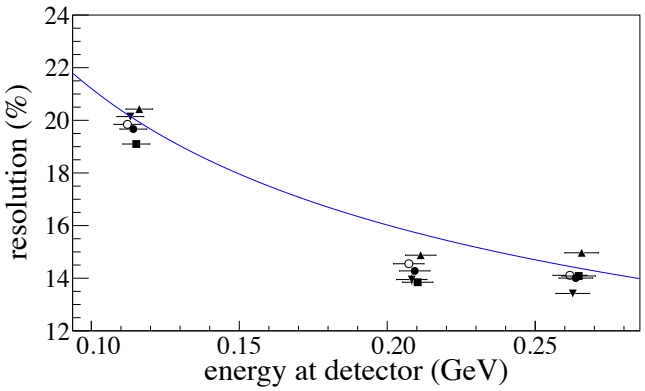


Figure 8: The energy resolution results against incoming energy. The different markers represent different trigger combination selections, and are slightly horizontally shifted for visual clarity. The solid blue curve is the expected resolution for GlueX.

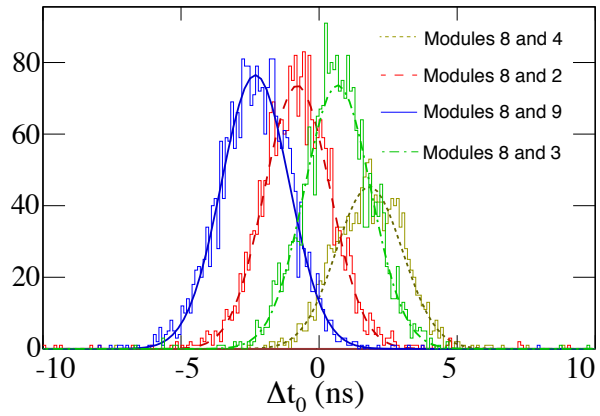


Figure 9: Distribution of $\Delta t_{0,ij}$ for a single module and four of its adjacent modules when all modules had $1000 < S_p < 2000$ ADC counts, together with Gaussian fit curves.

that was taken at an incoming electron energy of approximately 1275 MeV. The timing resolution depends strongly on the PMT signal amplitude, and the runs at this energy allowed us to measure the timing resolution across the largest range of sample pulse heights.

4.1. Timing resolution method

An example of the digitized PMT signal by the fADCs was shown in Fig. 6. We use the time at which the pulse reaches half the recorded maximum to specify the signal arrival time. This time, which we call t_0, is chosen because it is in the region of maximum slope.

The timing resolution was determined using a linear interpolation method, which assumes that we can approximate the signal shape between adjacent samples of the fADC linearly, a valid approximation on the leading edge of the pulse. We determined t_0 by interpolating the sample before and the sample after the halfway point of the maximum sample. Generally, the incoming electron in the beam test illuminated several blocks simultaneously, allowing us to compute the difference in t_0 for several different modules. We define the timing difference between two modules as $\Delta t_{0,ij} = t_{0,i} - t_{0,j}$, where $t_{0,i}$ is the signal arrival time t_0 for the ith module.

In principle we can compute the timing difference between any two modules, but since we are interested in determining the resolution for two modules with comparable signal amplitudes, we restricted ourselves to measurements of differences between adjacent modules, modules that are either side by side or diagonally aligned with the corners touching. Figure 9 shows the distribution of the timing difference $\Delta t_{0,ij}$ for a single module and four of its adjacent modules. Previous studies showed that the timing resolution depends strongly on the maximum pulse amplitude S_p, so the data were binned by requiring that for a given event, S_p for both modules were within the same range. For example in Fig. 9, the range of S_p was restricted to be between 1000 and 2000 ADC counts for the two modules.

4.2. Determination of timing resolution

For each range of S_p, the distribution of $\Delta t_{0,ij}$ was determined for all adjacent module combinations. Fits to each distribution were done with Gaussian functions, such as those shown in Fig. 9, to characterize each $\Delta t_{0,ij}$, which yield the resolution in timing difference σ_{ij} with statistical error $\delta\sigma_{ij}$. Fig. 10 shows how the σ_{ij} between a given module and four of its adjacent modules changes with S_p. Clearly the timing resolution improves with larger pulse amplitude.

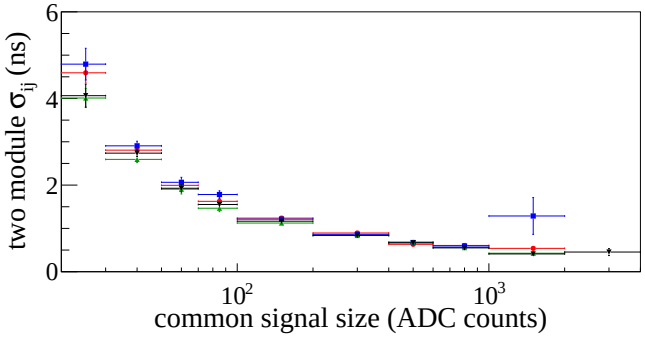


Figure 10: σ_{ij} between an example module and four of its adjacent modules, determined by fits such as those shown in Fig. 9. The four different colors and symbols represent different combinations of modules. Note the log scale on the x-axis.

The value σ_{ij} is the resolution on the difference in absolute time between two modules and is therefore worse than the time resolution for a single module. We assumed that the resolution of each single module σ_i contributes in quadrature to the observed timing difference resolution so that $\sigma_{ij}^2 = \sigma_i^2 + \sigma_j^2$, and determined each module's resolution from all of the different combinations measured. To do this, we divided our modules into 2×2 clusters where all modules within the cluster were adjacent to each other. Within a single cluster there are six possible separate measurements of timing differences. If all six combinations each had sufficient statistics to yield a fit result,

we did a fit to minimize

$$\chi^2 = \sum_{i,j>i} \left(\frac{\sigma_{ij} - \sqrt{\sigma_i^2 + \sigma_j^2}}{\delta\sigma_{ij}} \right)^2, \quad (2)$$

where the fit variables σ_i gave the intrinsic timing resolution of module i. This allowed a determination of the resolution of each module within that cluster.

Figure 11 shows the resolution of a single module. Because each module can be contained in up to four separate clusters, the timing resolution in a given bin of S_p can be determined up to four times. When there were multiple measurements coming from different clusters at a given range of S_p, the different measurements were merged by a weighted average, with the standard deviation taken as the error. We parametrized the results with fits of the form

$$\sigma(S_p) = \frac{a}{S_p} + b, \quad (3)$$

where a (ns · ADC counts) and b (ns) are fit parameters. Fits were also tried with other forms, such as $a/\sqrt{S_p} + b$ and $a/S_p \oplus b$, where in the latter form the two terms were added in quadrature, but neither of these fit the data better than Eq. (3).

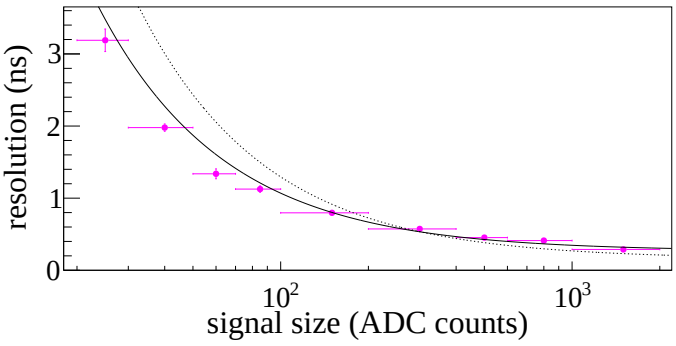


Figure 11: Final timing resolution for one module. The solid magenta points are the weighted averages and standard deviations of up to four separate clusters that determined the resolution for this module. The solid curve shows the fit result, while the dotted curve is from Ref. [13].

By fitting the timing resolution as a function of S_p, we determined the parameters a and b for each module. Table 2 shows the results of the parameters a and b for the six modules we used. By taking the average and standard deviation, our final results were $a = 72.9 \pm 5.3$ (ns·ADC counts), $b = 0.29 \pm 0.02$ (ns). We can convert the ADC counts into pulse heights in mV: the fADCs used 12 bits to digitize the 0.5 V fADC full scale. With this conversion, the fit parameter a becomes $a = 8.90 \pm 0.65$ ns · mV. We note that, on average, the gain of the modules is such that a signal pulse amplitude of 3 ADC counts corresponds to 1 MeV of deposited energy in a block.

The results from Ref. [13] gave the fit parameters $a = 114 \pm 46$ (ns · ADC counts), $b = 0.155 \pm 0.077$ (ns). The statistical parameter can be converted to pulse height with the 1.45 V fADC full scale used, and gives $a = 40.4 \pm 16.3$ ns · mV. For pulse heights of 100 mV and 500 mV, the timing resolutions are then 0.57 ± 0.18 ns, and 0.24 ± 0.08 ns, respectively. In the current measurements the actual pulse heights were limited to less than approximately 250 mV, but extrapolating our fit results gives timing resolutions of 0.38±0.03 ns and 0.30±0.02 ns for 100 mV and 500 mV pulses, respectively. Our results show that the timing resolution exceeded expectations at smaller signal amplitudes where previous results do not exist.

Table 2: Measurements of timing resolution parameters a and b from Eq. (3). The final row shows the average values and standard deviations of the six modules used.

Module number	a (ns · ADC counts)	b (ns)
7	77.9 ± 8.5	0.27 ± 0.02
8	65.6 ± 6.7	0.32 ± 0.02
9	78.9 ± 8.1	0.31 ± 0.02
12	68.1 ± 6.8	0.31 ± 0.02
13	72.5 ± 7.7	0.28 ± 0.02
14	74.6 ± 7.8	0.28 ± 0.02
Average	**72.9 ± 5.3**	**0.29 ± 0.02**

In the GlueX experiment, a single photon can cause showers in multiple blocks, which allow independent timing measurements from each block. Combining these measurements will further enhance the timing resolution of photon showers, thereby enhancing our ability to choose which beam bunch produced the signal photon of interest and reject background electromagnetic showers.

5. Conclusions

Results of a beam test using a small version of the FCAL of the GlueX experiment are given. The energy resolution is between 14% and 20% at energies of 260 MeV down to 110 MeV. This represents the first test of the production calorimeter hardware and electronics with actual electromagnetic showers. The energy resolution is consistent with the design goals for GlueX at these low energies. Precision timing measurements of the FCAL signals is a feature that is possible due to the 250 MHz fADCs to be used in GlueX. The timing resolution is found to exceed the expectations of previous measurements at low PMT pulse amplitudes, with timing resolutions of 0.38 ns and better achievable from a single module with signals larger than 100 mV. A weighted average of timing measurements from different modules that are illuminated by a single shower will allow enhanced precision of shower time allowing a determination of the beam bunch and a rejection of out-of-time electromagnetic background.

Acknowledgments

We would like to thank the CLAS Collaboration and the members of the HD-ICE experiment, for their hospitality, time and effort, which made our beam test possible. We would especially like to thank Eugene Pasyuk and Sergey Boyarinov for

their help. This work was supported by the Department of Energy under contract DE-FG02-05ER41374. Jefferson Science Associates, LLC operated Thomas Jefferson National Accelerator Facility for the United States Department of Energy under contract DE-AC05-06OR23177.

References

[1] https://www.jlab.org/Hall-D
[2] https://www.jlab.org/Hall-B
[3] A. Brunner et al., A Cockcroft-Walton base for the FEU84-3 photomultiplier tube, Nuclear Instruments and Methods in Physics Research A 414 (1998) 466. doi:10.1016/S0168-9002(98)00651-2
[4] http://lzos.ru/
[5] H. Dong et al., Integrated tests of a high speed VXS switch card and 250 MSPS flash ADCs, Nuclear Science Symposium Conference Record, 2007. NSS '07. IEEE, Vol. 1, 2007, pp. 831-833. doi:10.1109/NSSMIC.2007.4436457
[6] B.B. Brabson et al., A Study of two prototype lead glass electromagnetic calorimeters, Nuclear Instruments and Methods in Physics Research A 332 (1993) 419. doi:10.1016/0168-9002(93)90299-W
[7] R.R. Crittenden et al., A 3000 element lead-glass electromagnetic calorimeter, Nuclear Instruments and Methods in Physics Research A 387 (1997) 377. doi:10.1016/S0168-9002(97)00101-0
[8] R.T. Jones et al., A bootstrap method for gain calibration and resolution determination of a lead-glass calorimeter, Nuclear Instruments and Methods in Physics Research A 566 (2006) 366. doi:10.1016/j.nima.2006.07.061
[9] R.T. Jones et al., Performance of the RADPHI detector and trigger in a high rate tagged photon beam, Nuclear Instruments and Methods in Physics Research A 570 (2007) 384. doi:10.1016/j.nima.2006.09.039
[10] D.I. Sober et al., The bremsstrahlung tagged photon beam in Hall B at JLab, Nuclear Instruments and Methods in Physics Research A 440 (2000) 263. doi:10.1016/S0168-9002(99)00784-6
[11] S.K. Matthews et al., A composite thin vacuum window for the CLAS photon tagger at Jefferson lab, Nuclear Instruments and Methods in Physics Research A 421 (1999) 23. doi:10.1016/S0168-9002(98)00910-3
[12] S.Agostinelli et al., GEANT4: A Simulation toolkit, Nuclear Instruments and Methods in Physics Research A 506 (2003) 250. doi:10.1016/S0168-9002(03)01368-8
[13] J.V. Bennett et al., Precision timing measurement of phototube pulses using a flash analog-to-digital converter, Nuclear Instruments and Methods in Physics Research A 622 (2010) 225. doi:10.1016/j.nima.2010.06.216